ARTICLE

Beyond the Roles in Biomimetic Chemistry: An Insight into the Intrinsic Catalytic Activity of an Enzyme for Tumor-Selective Phototheranostics

Weitao Yang,[†] Xiudong Shi,[‡] Yuxin Shi,[‡] Defan Yao,[†] Shizhen Chen,[§] Xin Zhou,[§] and Bingbo Zhang*,[†]

[†]Institute of Photomedicine, Shanghai Skin Disease Hospital, The Institute for Biomedical Engineering and Nano Science, Tongji University School of Medicine, Shanghai 200443, China

[‡]Department of Radiology, Shanghai Public Health Clinical Center, Fudan University, Shanghai 201508, China

[§]Key Laboratory of Magnetic Resonance in Biological Systems, State Key Laboratory of Magnetic Resonance and Atomic and Molecular Physics, National Center for Magnetic Resonance in Wuhan, Wuhan Institute of Physics and Mathematics, Chinese Academy of Sciences, Wuhan 430071, China

S *Supporting Information*

ABSTRACT: Protein-assisted biomimetic synthesis has been an emerging offshoot of nanofabrication in recent years owing to its features of green chemistry, facile process, and ease of multi-integration. As a result, many proteins have been used for biomimetic synthesis of varying kinds of nanostructures. Although the efforts on exploring new proteins and investigating their roles in biomimetic chemistry are increasing, the most essential intrinsic properties of proteins are largely neglected. Herein we report a frequently used enzyme (horseradish peroxidase, HRP) to demonstrate the possibility of enzymatic activity retaining after accomplishing the roles in biomimetic synthesis of ultrasmall gadolinium (Gd) nanodots and stowing

its substrate 2,2′-Azinobis (3-ethylbenzothiazoline-6-sulfonic acid ammonium salt) (ABTS), denoted as Gd@HRP^{ABTS}. It was found that *ca.* 70% of the enzymatic activity of HRP was preserved. The associated changes of protein structure with chemical treatments were studied by spectroscopic analysis. Leveraging on the highly retained catalytic activity, Gd@HRP^{ABTS} exerts strong catalytic oxidation of peroxidase substrate ABTS into photoactive counterparts in the presence of intrinsic H_2O_2 inside the tumor, therefore enabling tumor-selective catalytic photoacoustic (PA) imaging and photothermal therapy (PTT). In addition, the MR moiety of Gd@HRP^{ABTS} provides guidance for PTT and further diagrams that Gd@HRP^{ABTS} is clearable from the body *via* kidneys. Preliminary toxicity studies show no observed adverse effects by administration of them. This study demonstrates beyond the well-known roles in biomimetic chemistry that HRP can also preserve its enzymatic activity for tumor catalytic theranostics.

KEYWORDS: *biomimetic synthesis, protein activity, catalytic nanomedicine, MR/PA imaging, photothermal therapy*
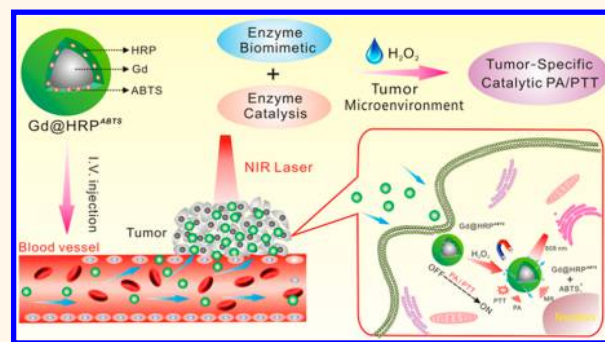
Simple and green technologies for synthesis of nanomaterials are essential to the advancement and translation of nanoscience and nanotechnology, especially for biomedical settings. Protein/peptide-mediated biomimetic synthesis has been recognized as such a kind of technology because it holds advantages of green synthetic route, ease of multifunctional integration, and biocompatibility.[1−4] To date, many proteins have been explored and used for biomimetically synthesizing a variety of nanomaterials.[5] Nevertheless, the major drawback for the reported biomimetic synthesis is that the intrinsic properties of proteins such as targeting, fluorescence, and enzymatic activity are largely overlooked after chemical reactions.

Nowadays, protein-mediated biomimetic strategy, though the synthesis mechanism is still not very clear, has widely attracted interests and emerged as a promising alternative in nanofabrication, especially in the biomedical field, where green

Scheme 1. Schematic Illustration of HRP-Assisted Biomimetic Synthesis of Ultrasmall Nanodots while Simultaneously Retaining High Enzymatic Activity for Tumor-Selective Catalytic Phototheranostics
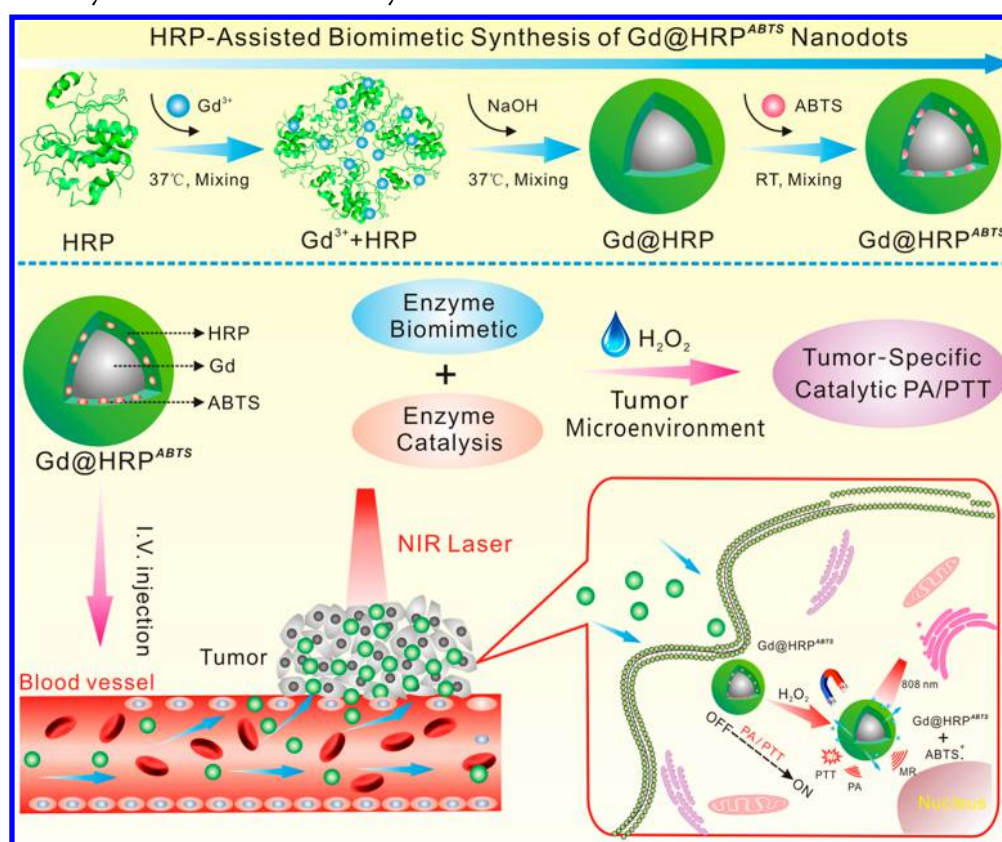
chemistry, ease of synthesis, and biocompatibility are highly demanded.[5,6] Considering these advantages, a series of nanoparticles have been reported for cancer theranostics. For instance, we used bovine serum albumin (BSA) to integrate MR imaging and photothermal moieties in a biomimetic manner for *in vivo* MR/photoacoustic (PA) imaging-guided phototherapy.[3] In addition, other nanoparticles, such as metal nanoclusters (AuNCs, AgNCs, PtNCs, CuNCs),[2,7] gold nanoparticles, tellurium nanodots,[8−10] metal oxide (MnO$_2$, Gd$_2$O$_3$, CeO$_2$),[11] and metal sulfide (Bi$_2$S$_3$, NiS, Ag$_2$S) nanoparticles,[1,12−14] and semiconducting polymer nanoparticles[15−19] were synthesized by other groups for *in vitro* diagnosis, cancer imaging, and therapy. More related work has been summarized in our previous reviews.[20,21]

Generally, in a biomimetic synthesis case, a protein plays multiple roles such as reducers, stabilizers, and reaction-zone providers. Obviously, the synthesis of these nanostructures is significantly simplified, and the resultants become more appealing for biomedical use. Despite these demonstrations, almost all the efforts are limited on exploring new proteins and incubating various types of nanostructures. The insight into the intrinsic properties of the proteins after biomimetic chemistry is sorely lacking.

In this study, we present an enzyme, horseradish peroxidase (HRP), which is frequently used for *in vitro* enzyme linked immunosorbent (ELISA), to demonstrate its remaining enzymatic activity for intelligent response, not just showing off its contribution in biomimetic synthesis. Compared with other reported proteins, such as albumin (BSA, HSA), transferrin, lactoferrin, and plant protein, HRP enzyme in this study still maintains high enzymatic activity after incubating high-quality

Gd nanodots and loading its substrate. The final product is denoted as Gd@HRP^{ABTS}. More than ever, HRP not only acts as an incubator, a stabilizer, and a carrier in the biomimetic chemistry but also can function as a catalyst for catalyzing the oxidizing reaction between the loaded substrate (ABTS) and hydrogen peroxide (H$_2$O$_2$). The preserved enzymatic activity was verified both *in vitro* and on tumor-bearing mice. In the tumor site, the photosilent ABTS was catalytically oxidized by HRP into the photosensitive counterpart ABTS•+, enabling tumor-selective PA imaging and PTT. Moreover, the tumor uptake, PTT treatment, and biodistribution are well monitored by the MR moiety of Gd@HRP^{ABTS} nanodots under the MR imaging mode. The synthesis and proof-of-concept application are illustrated in Scheme 1.

RESULTS AND DISCUSSION

Biomimetic Synthesis and Characterizations of Gd@HRP^{ABTS} Nanodots. Paramagnetic Gd@HRP^{ABTS} nanodots were synthesized by a facile enzyme-biomimetic route, which is depicted in Scheme 1. HRP plays multiple roles in these biomimetic processes: as biotemplate for nanodots formation, substrate (ABTS) loading, and catalyst for PA/PTT. The main physicochemical properties of Gd@HRP^{ABTS} nanodots were investigated. As shown the typical HRTEM image in Figure 1A, the synthesized Gd@HRP^{ABTS} nanodots display a spherical structure with an ultrasmall size of *ca.* 4.0 nm. The corresponding hydrodynamic size (HDs) is *ca.* 7.5 nm (Figure 1B), which is larger than the TEM result mainly due to HRP encapsulation. We optimized the ratio of HRP to Gd ions in the synthesis of Gd@HRP nanodots. When the amount of HRP was set as 5 mg, a large number of precipitates appeared in the
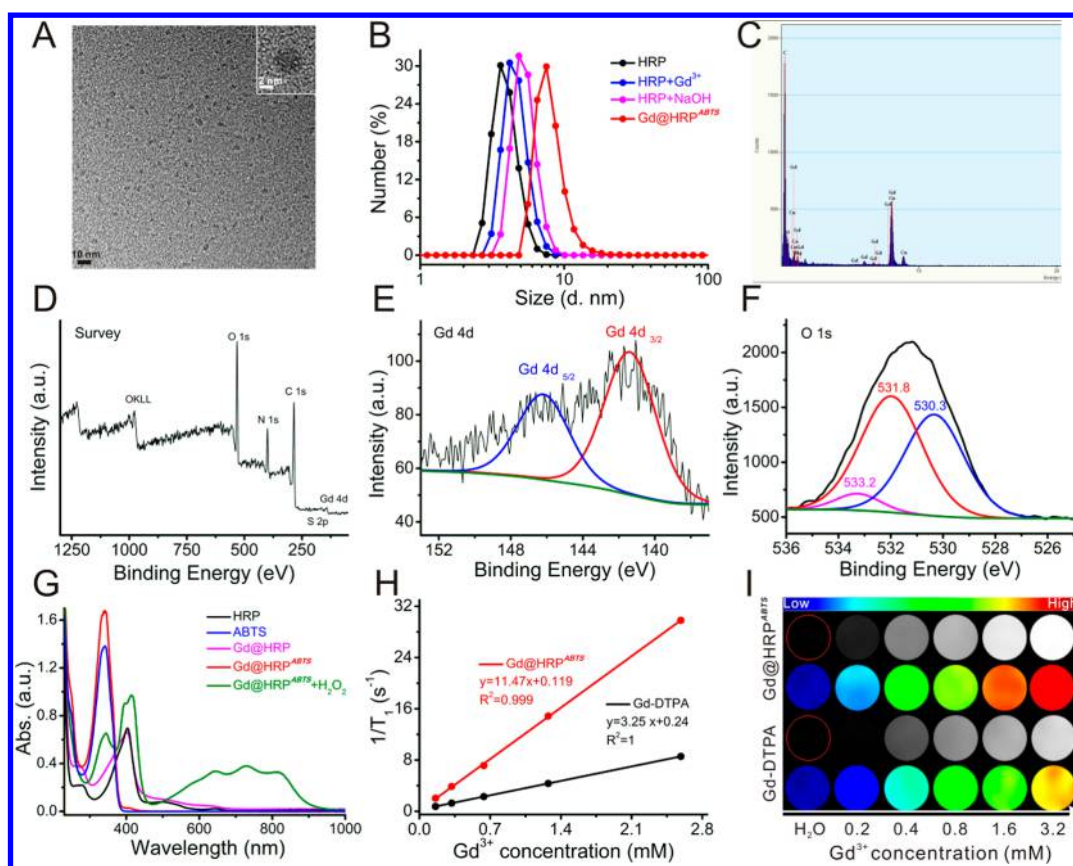
Figure 1. Synthesis and characterizations of Gd@HRP[ABTS] nanodots. (A) Representative TEM and HRTEM images (the inset) of Gd@HRP[ABTS] nanodots. The scale bar is 10 and 2 nm, respectively. (B) The hydrodynamic sizes of HRP, HRP + Gd^{3+}, HRP + NaOH, and Gd@HRP[ABTS] nanodots. (C) EDS spectrum of Gd@HRP[ABTS]. (D) XPS survey spectrum of Gd@HRP[ABTS], (E) Gd 4d, and (F) O 1s XPS spectra and their corresponding fitting curves obtained by using XPS Peak 4.1 software. (G) The UV−vis absorption spectra of HRP, ABTS, Gd@HRP, and Gd@HRP[ABTS] before and after H_2O_2 treatment. (H) The longitudinal relaxation curve fitting and (I) *in vitro* T_1-weighted MR images of Gd@HRP[ABTS] and the commercial contrast agent (Magnevist, Gd-DTPA).

reaction system, which indicates the amount of HRP was too little to bind the Gd^{3+} and stabilize the nanoparticles. Upon increasing the HRP amount, a stable and clear solution was obtained. The corresponding HDs were measured and are shown in Figure S1, Supporting Information.

EDS and XPS analyses were conducted to confirm the composition of nanodots. As shown in Figure 1C,D, both clearly confirm the existence of Gd element. Gd (4d) and O (1s) peaks were analyzed by using XPS Peak 4.1 software to confirm their definite chemical states in the formed nanodots. As shown in Figure 1E, the peaks centered at 141.3 eV (Gd 4d 3/2) and 146.2 eV (Gd 4d 5/2) in Gd 4d spectrum are assigned to Gd $(OH)_3$ and Gd_2O_3, respectively. Peaks centered at 532.096, 530.909, and 532.6 eV in Figure 1F are the characteristics of oxygen in Gd$(OH)_3$ and Gd_2O_3 and the oxygen in −COOH and −OH of HRP molecules.[3,22−25] The UV−vis absorption spectrum of Gd@HRP[ABTS] in Figure 1G shows the characteristic peak at 342 nm of ABTS, which indicates the successful loading of ABTS. According to the linear fitting curve obtained by the standard ABTS concentration *versus* absorption at 342 nm, the loaded ABTS on HRP can be calculated to be 3.3% (Figure S2, Supporting Information). Moreover, it was found in the UV−vis absorption spectra that a trace of H_2O_2 can significantly arouse the absorption of nanodots in the NIR region (Figure 1G, green curve) with a color change from brown to dark green (Figure S3, Supporting Information), demonstrating an ultrasensitive

response of Gd@HRP[ABTS]. Additional data on the response study are displayed below.

To evaluate the T_1-weighted MR imaging ability of Gd@HRP[ABTS] nanodots, the longitudinal (T_1) and transverse (T_2) relaxation times were measured at different Gd^{3+} concentrations, respectively. As presented in Figure 1H and Figure S4 in Supporting Information, the longitudinal (r_1) and transverse (r_2) relaxation rates of Gd@HRP[ABTS] nanodots were calculated to be 11.47 mM[−1]·s^{−1} and 19.23 mM[−1]·s^{−1}, respectively, which is nearly four times as high as that of commercial agent (Gd-DTPA, r_1 = 3.25 mM[−1]·s^{−1}). According to the Solomon−Bloembergen−Morgan theory and previous studies,[26−29] there are three key factors that affect the longitudinal relaxivity: (1) the number of water molecules directly coordinated to the paramagnetic metal ions (q), (2) molecular rotational correlation time (τ_R), and (3) proton residence lifetime (τ_m). Generally, longer τ_R and larger q are expected to improve the longitudinal relaxivity of contrast agents. For Gd@HRP[ABTS] nanodots, the proper size of 4.0 nm could provide high a surface-to-volume ratio for sufficient water−metal interactions and thus obtain a big q. Furthermore, the encapsulation of biomacromolecule (HRP) brings about a longer rotational correlation time (τ_R), leading to enhanced relaxivity. However, for Gd-DTPA, only one coordination site opens up for water coordination, and the molecular rotational correlation time of Gd^{3+} on small molecule (DTPA) is much shorter than that on the HRP biomacromolecule. In addition, the r_2/r_1 ratio was calculated to
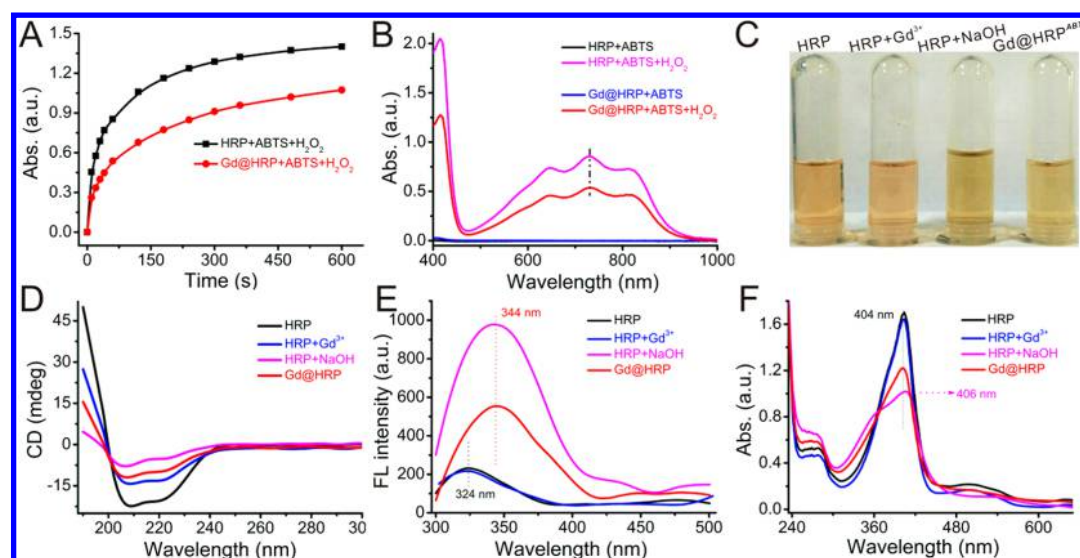
Figure 2. Enzymatic activity and protein structure analysis of HRP before and after biomimetic synthesis. (A) Time-dependent absorbance at 730 nm of free HRP and Gd@HRP with the same content of HRP (0.2 mg/mL) after incubation with ABTS (0.274 mg/mL) and H_2O_2 (100 μM). (B) The representative UV−vis absorbance spectra after 1 min of incubation. Digital photos (C), circular dichroism (D), intrinsic protein fluorescence (E), and UV−vis absorbance spectra (F) of HRP before and after different treatments.

be 1.8, which is below 3, suggesting Gd@HRP^{ABTS} nanodots favor T_1-weighted MR imaging.[30] Subsequently, the *in vitro* T_1-weighted MR images (Figure 1I) and the corresponding signal intensity at the same Gd^{3+} concentration (Figure S5, Supporting Information) are provided, and they further indicate that the Gd@HRP^{ABTS} nanodots can produce a stronger MR signal (300%, compared with H_2O) than commercial agent (Gd-DTPA). All of these collectively indicate that Gd@HRP^{ABTS} is a highly efficient T_1-weighted MR contrast agent.

Enzymatic Activity and Protein Structure Study of Gd@HRP^{ABTS}. The enzymatic activity of HRP in the Gd@HRP nanodots is very critical for the following biomedical PA/PTT applications. Based on the previous reports, the oxidation of ABTS by H_2O_2 can be catalyzed to be ABTS•+ in the presence of HRP by the following reaction equation:[31,32]

$$ABTS + 1/2H_2O_2 \rightarrow ABTS\bullet+ 1/2H_2O$$
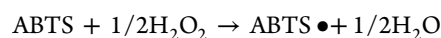
This oxidation can transfer the photosilent ABTS into photoactive ABTS•+, which has strong NIR absorption and photothermal conversion efficiency. However, the issue of this study is whether the chemical reaction could quench the enzymatic activity of HRP or not. Hence, we dynamically compared the enzymatic activities of the free HRP and the synthesized Gd@HRP by adding ABTS and H_2O_2. As shown in Figure 2A, in the presence of H_2O_2, time-dependent observation of absorptions in the NIR region (734 nm) indicates good catalytic oxidation performance of both free HRP and Gd@HRP. However, a slightly weaker increase triggered by Gd@HRP is observed compared to that by the free HRP. According to the UV−vis absorption spectra (Figure 2A,B), it could be roughly calculated that approximately 70% of the HRP activity was maintained after synthesis.

To find out what happened during or after chemical reaction, we prepared solutions of free HRP, HRP + Gd^{3+}, HRP + NaOH, and the as-synthesized Gd@HRP for analysis and comparison. First, the appearances of each solution were photographed as exhibited in Figure 2C. It was found that there was no obvious color change in the group of free HRP and HRP + Gd^{3+}, neither in the group of HRP + NaOH and the as-synthesized Gd@HRP.

However, there is a slight color change between these two groups. Considering the difference in chemical process between these two groups is just the involvement of NaOH, thus we speculate that the most potential inducement is the addition of NaOH.

Subsequently, we compared the circular dichroism (CD) spectra of HRP, HRP + Gd^{3+}, HRP + NaOH, and Gd@HRP to examine the secondary structure change before and after synthesis. As displayed in Figure 2D, two negative characteristic peaks at 208 and 222 nm representing the α helix structure of HRP appear in all four samples without any wavelength shift. However, the intensities of these two peaks turn weaker and weaker from the order of free HRP, HRP + Gd^{3+}, Gd@HRP to HRP + NaOH, suggesting the α helix structure content in the samples decreases accordingly. We noticed that the intensity in Gd@HRP is stronger than that in HRP + NaOH, indicating the α helix structure of HRP can be partially recovered after removal of NaOH. (Note: The sample of Gd@HRP was purified by dialysis and redispersed in pure water for analysis.) This finding agrees well with that observed on the color appearance of each solution, both pointing to the critical effect of NaOH.

To further study the structure change, the intrinsic protein fluorescence and UV−vis absorption spectra were measured. The intrinsic protein fluorescence predominantly derived from tryptophan is usually applied to study protein conformational changes. The fluorescence pattern of tryptophan, namely the wavelength and intensity, is strongly influenced by its (or the protein's) local microenvironment. As shown in Figure 2E, there is no observed fluorescence difference in the group of HRP + Gd^{3+} and the free HRP, suggesting Gd^{3+} ions could not affect the structure of HRP. The conservative effect of Gd^{3+} ions on HRP is also reflected by the same color between these two samples in the Figure 2C. However, the peak at 324 nm is red-shifted to 344 nm in the samples of Gd@HRP and HRP + NaOH, mainly attributed to the structure change and the increased polarity of the tryptophan microenvironment.[33] Moreover, the sample of HRP + NaOH shows almost twice the fluorescence intensity of Gd@HRP. It seems to imply that once again NaOH plays a crucial role in these changes. It could produce a stronger polar
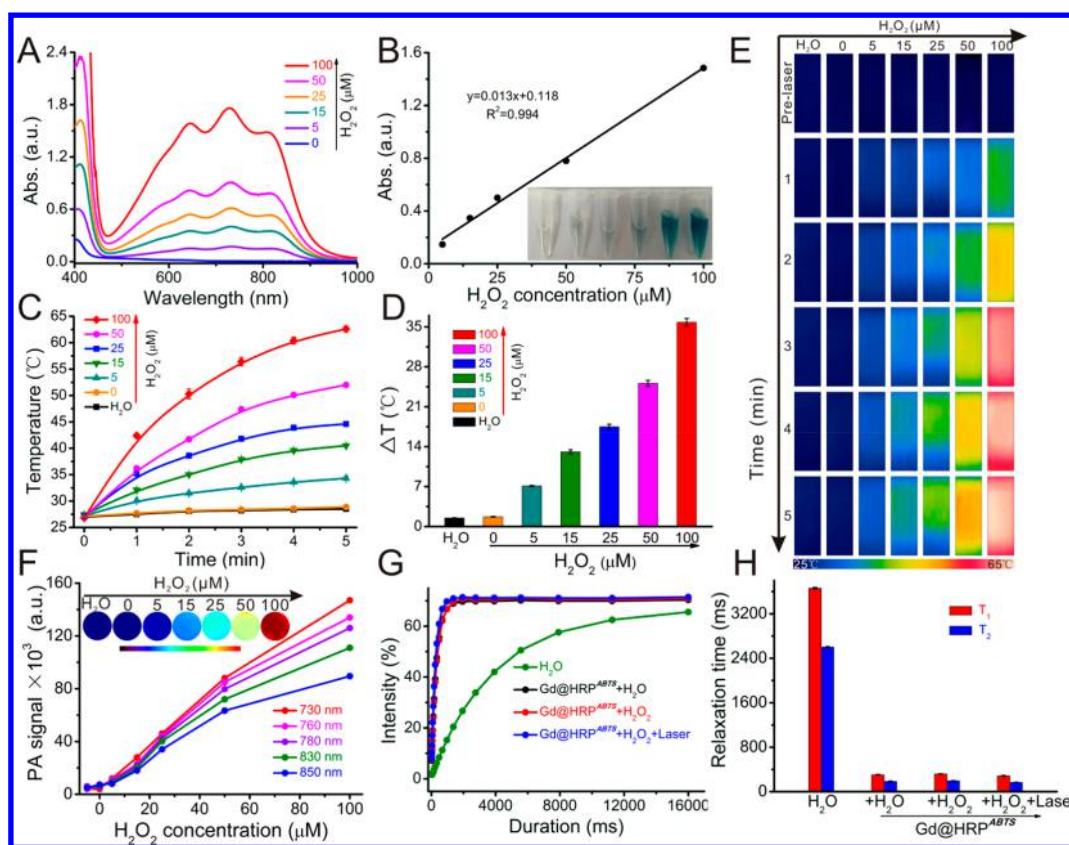
Figure 3. Response performance studies of Gd@HRP^{ABTS} nanodots toward H_2O_2. (A) The UV−vis absorption spectra of Gd@HRP^{ABTS} nanodots before and after different concentrations of H_2O_2 treatments ($0-100\,\mu$M). (B) The linear fitting curve between H_2O_2 concentration and the absorbance at 808 nm. (C) Time-dependent temperature incensement curve of Gd@HRP^{ABTS} nanodots before and after different concentrations of H_2O_2 treatments ($0-100\,\mu$M) under laser irradiation (808 nm, 1.0 W/cm^2). (D) Temperature increase (ΔT) *versus* H_2O_2 concentration. (E) The corresponding infrared thermal images. (F) PA signal intensity of Gd@HRP^{ABTS} nanodots before and after different concentrations of H_2O_2 treatments ($0-100\,\mu$M) under different wavelength of laser irradiation (730 nm-850 nm). Inset: the corresponding PA images. (G) The T_1-weighted relaxation curves and (H) relaxation times of H_2O, Gd@HRP^{ABTS} nanodots, Gd@HRP^{ABTS} + H_2O_2, and Gd@HRP^{ABTS} + H_2O_2 + laser irradiation.

microenvironment for the emission of tryptophan. However, removal of NaOH from samples after synthesis helps recover the structure and reduce the polarity. These findings agree very well with those found in the above CD spectra and the color appearance.

The above four samples were further investigated by using UV−vis absorption spectrum measurement. As shown in Figure 2F, quite similar results to intrinsic fluorescence are obtained. Gd^{3+} ions addition could not affect the absorption spectrum pattern, while NaOH addition can decrease the absorption at 404 nm and produce a 2 nm of red-shift. These changes in absorption intensity and wavelength can be also recovered by removing NaOH.

As can be seen from the above data, Gd^{3+} ions have a slight effect on the protein conformation of HRP, while the strong alkalinity triggered by NaOH exerts much bigger impact on the conformation of HRP. Interestingly, this change or enzymatic activity can be recovered by removing NaOH, like dialysis for several hours against distilled water. Taken together, although the structure or the conformation of HRP undergoes a slight change after chemical reaction, its activity is still well retained and found strong enough for catalytic applications.

Response Performance Study of Gd@HRP^{ABTS} Nanodots Toward H_2O_2. Upon confirming the good residual of enzymatic activity of HRP after Gd@HRP synthesis, we further stuffed ABTS into Gd@HRP, therefore the integrated

theranostic Gd@HRP^{ABTS} nanodots were achieved. The related data for claiming successful loading is already provided in Figure 1G.

To verify the enzymatic catalysis process, UV−vis absorption spectra of Gd@HRP^{ABTS} before and after addition of H_2O_2 were measured. As displayed in Figure 3A, with the increase of H_2O_2 concentration, the absorbance of Gd@HRP^{ABTS} at NIR region significantly enhances, and it presents a linear dependence with a certain H_2O_2 concentration ($0-100\,\mu$M) (Figure 3B). The response concentration of the added H_2O_2 can be as low as 5 μM. The corresponding color of the reaction solution changes rapidly (a few seconds) and gradually from colorless to dark green upon the addition of different amounts of H_2O_2.

Leveraging on the enhanced absorbance in the NIR window after catalysis reaction, H_2O_2 concentration-dependent photothermal conversion effect was conducted. As displayed in Figure 3C−E, the temperature of Gd@HRP^{ABTS} can reach over 60 °C after 5 min of laser irradiation (808 nm, 1.0 W/cm^2). As expected, the increase of temperature is positively related to the added amount of H_2O_2. Because Gd@HRP^{ABTS} can produce heat in the presence of H_2O_2 effectively, we further applied these nanodots for PA imaging. As shown in Figure 3F, it was found that Gd@HRP^{ABTS} generates the strongest PA signal intensity at 730 nm, which agrees with the maximum absorption peak observed above, and the PA imaging effect is also positively correlated with the H_2O_2 concentration ($0-100\,\mu$M).
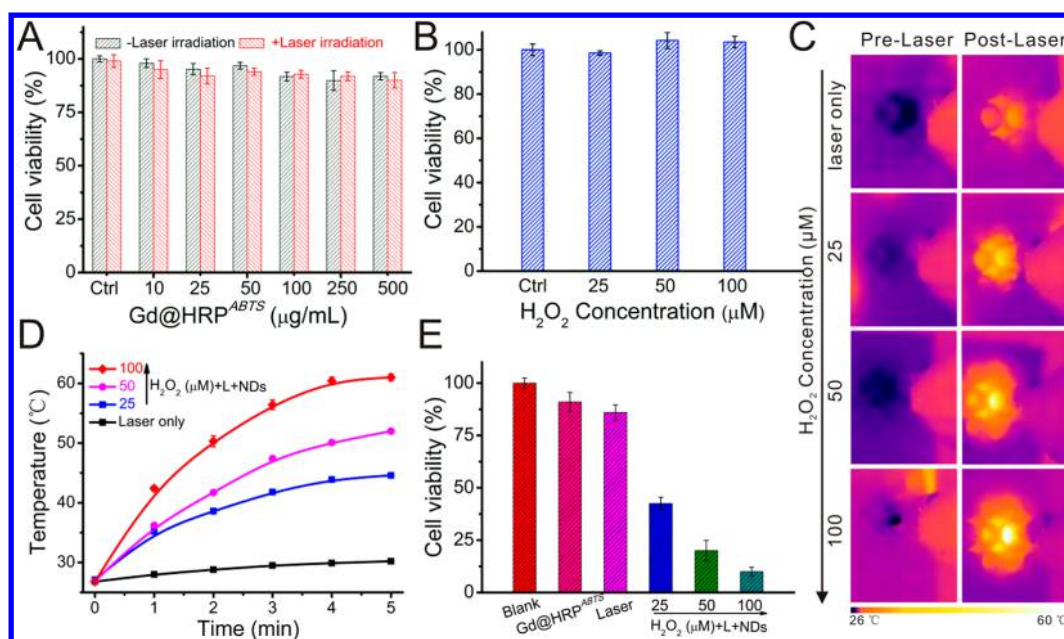
Figure 4. Cytotoxicity and H_2O_2-triggered phototherapy of Gd@HRP^{ABTS} nanodots. The 4T1 cell viability after incubation with different concentrations of (A) Gd@HRP^{ABTS} nanodots (0−500 μg/mL) before and after laser irradiation and (B) H_2O_2 (0−100 μM) for 24 h. (C) Thermal images of cells treated with laser only and Gd@HRP^{ABTS} nanodots + H_2O_2 (25−100 μM) + laser, (D) corresponding temperature incensement curve, and (E) the cell viabilities.
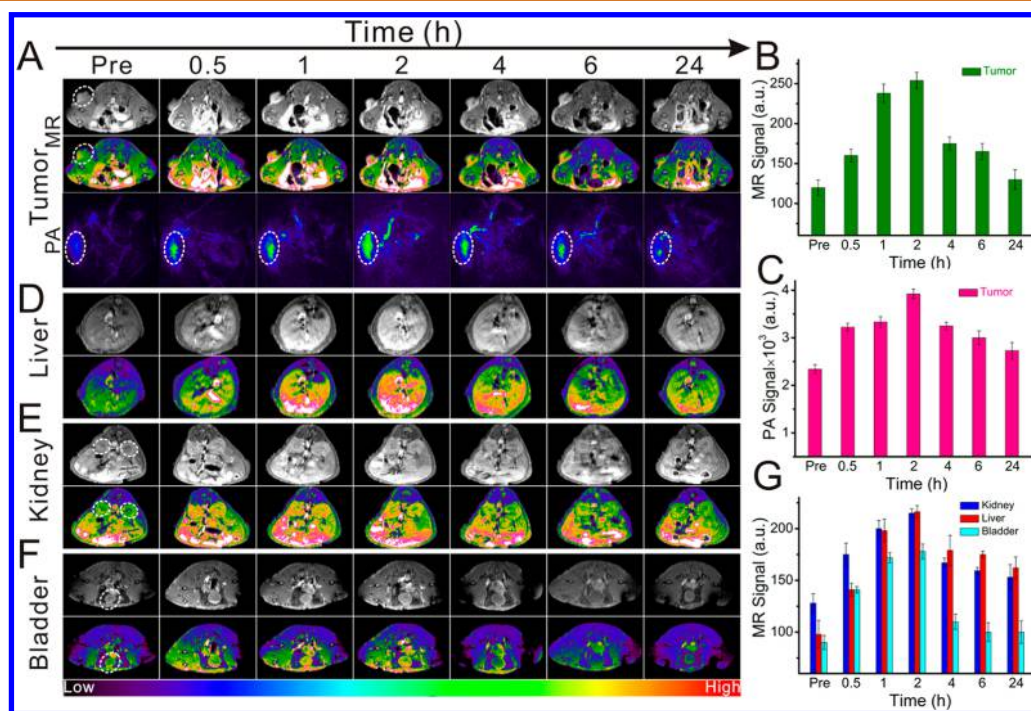

Figure 5. *In vivo* MR imaging guidance and H_2O_2-triggered PA imaging in tumor-bearing mice. (A) Time-dependent *in vivo* MR and corresponding PA imaging of tumor before and after intravenous injection of Gd@HRP^{ABTS} nanodots (dose: 0.08 mmol Gd/kg). (B) The corresponding T_1-weighted MR signal and (C) PA signal intensities of tumor before and after intravenous injection of Gd@HRP^{ABTS} nanodots. (D−F) *In vivo* MR imaging of Gd@HRP^{ABTS} nanodots, including in the (D) liver, (E) kidneys, and (F) bladder. (G) The corresponding MR signal intensities of liver, kidney, and bladder.

In addition, the MR imaging capability and photostability of Gd@HRP^{ABTS} before and after treatment with H_2O_2 and NIR laser irradiation were investigated, respectively. As displayed in Figure S6 (Supporting Information), the relaxation curve and relaxation time of Gd@HRP^{ABTS} without H_2O_2 are very stable even after laser irradiation for 24 h. After reaction with H_2O_2, the

absorption at NIR light was activated, and we also found the relaxation time still stays constant (Figure 3G,H), which can be attributed to the strong encapsulation of HRP for Gd nanodots.

Furthermore, the enzymatic activity of Gd@HRP^{ABTS} after laser irradiation was evaluated by re-adding the fresh substrate (ABTS) and H_2O_2, followed by monitoring the absorption
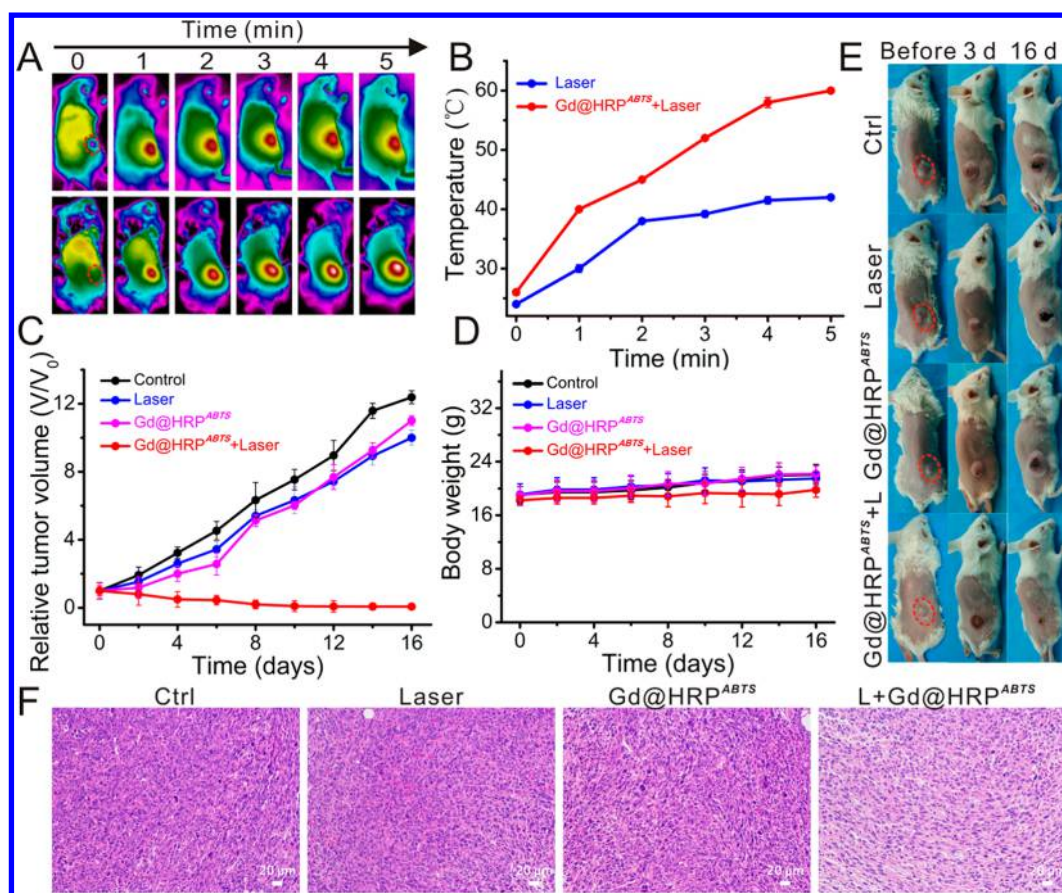
Figure 6. *In vivo* H_2O_2-tiggered catalytic PTT in tumor-bearing mice. (A) Thermal images of 4T1 tumor-bearing mice before and after intravenous injection of physiological saline and Gd@HRP[ABTS] nanodots, followed by an 808 nm laser irradiation for 5 min, respectively. (B) The curves of tumor temperature *versus* irradiation time. (C) Digital pictures of mice in different groups before and after 3 days and 16 days of PTT. (D) The relative tumor volumes and (E) body weight changes of mice in different groups (control, laser only, Gd@HRP[ABTS] nanodots only, and Gd@HRP[ABTS] nanodots + laser irradiation) during PTT. (F) H&E-stained tumor tissue slices collected from different groups including physiological saline, laser only, Gd@HRP[ABTS] nanodots only, and Gd@HRP[ABTS] nanodots + laser irradiation.

spectrum of the mixture solution. It was found that the absorption peak can still increase compared with that before laser irradiation (Figure S7, Supporting Information). This suggests that the heated HRP can still catalyze ABTS into ABTS•+ after laser irradiation. It should be noted that here the temperature for this enzymatic activity evaluation was controlled at 56 °C, which is the same as for the tumor PTT therapy.

Cytotoxicity Study and *in Vitro* H_2O_2-Triggered PTT. CCK-8 assay was conducted to assess the cytotoxicity of Gd@HRP[ABTS] nanodots on 4T1 breast cancer cells. After incubating with Gd@HRP[ABTS] and commercial Gd-DTPA at varying concentrations (10 μg/mL, 25 μg/mL, 50 μg/mL, 100 μg/mL, 250 μg/mL, and 500 μg/mL) at 37 °C under 5% CO_2 for 24 h, it was found that cell viability can exceed 80% even at concentration of 500 μg/mL, confirming the low toxicity of Gd@HRP[ABTS] and Gd-DTPA. And the laser irradiation has no significant effect on cell viability (Figure 4A and Figure S8, Supporting Information). In addition, the cytotoxicity of H_2O_2 was evaluated (Figure 4B), and we found negligible cytotoxicity of H_2O_2 even at 100 μM, which is in accord with the previous reports.[34,35]

Subsequently, the *in vitro* H_2O_2-triggered PTT was investigated. As shown in Figure 4C,D, the temperature of the cells treated with Gd@HRP[ABTS] nanodots increases significantly up to ∼60 °C at 100 μM of H_2O_2 after laser irradiation for 5 min, while the temperature of the cells treated by laser irradiation

only just improves from 26 to 31 °C. Compared with the control groups, including the cells without any treatment, with Gd@HRP[ABTS] nanodots only, and with the laser only, the cells treated with Gd@HRP[ABTS] nanodots plus laser irradiation were found burned in varying degrees in the presence of varying concentrations of H_2O_2, showing about 90% of the 4T1 breast cancer cells are killed by the 100 μM of H_2O_2-triggered thermal effect (Figure 4E). These studies demonstate that the Gd@HRP[ABTS] nanodots are quite safe to cells, but they become pretty toxic when H_2O_2 involved.

***In Vivo* MR Imaging Guidance and H_2O_2-Triggered PA Tumor Imaging.** In this study, we intentionally incorporate the Gd element to provide nanodots with MR imaging guidance capability during PTT. *In vitro* MR measurements as illustrated in Figure 1H,I show a good relaxivity property in Gd@HRP[ABTS] nanodots. *In vivo* MR imaging on living mice, as displayed in Figure 5A,B, shows a large accumulation of Gd@HRP[ABTS] nanodots in the tumor at 1 h post-intravenous injection. The MR imaging clearly illustrates that the tumor is gradually enhanced, and after 2 h, the signal in tumor starts to decrease. Compared with the commercial MR contrast agent (Gd-DTPA), the imaging time window is significantly prolonged to 1−2 h from several minutes, which is of clinical significance for the guidance or monitoring of tumor treatment. More importantly, this extended retention time in tumor undoubtedly
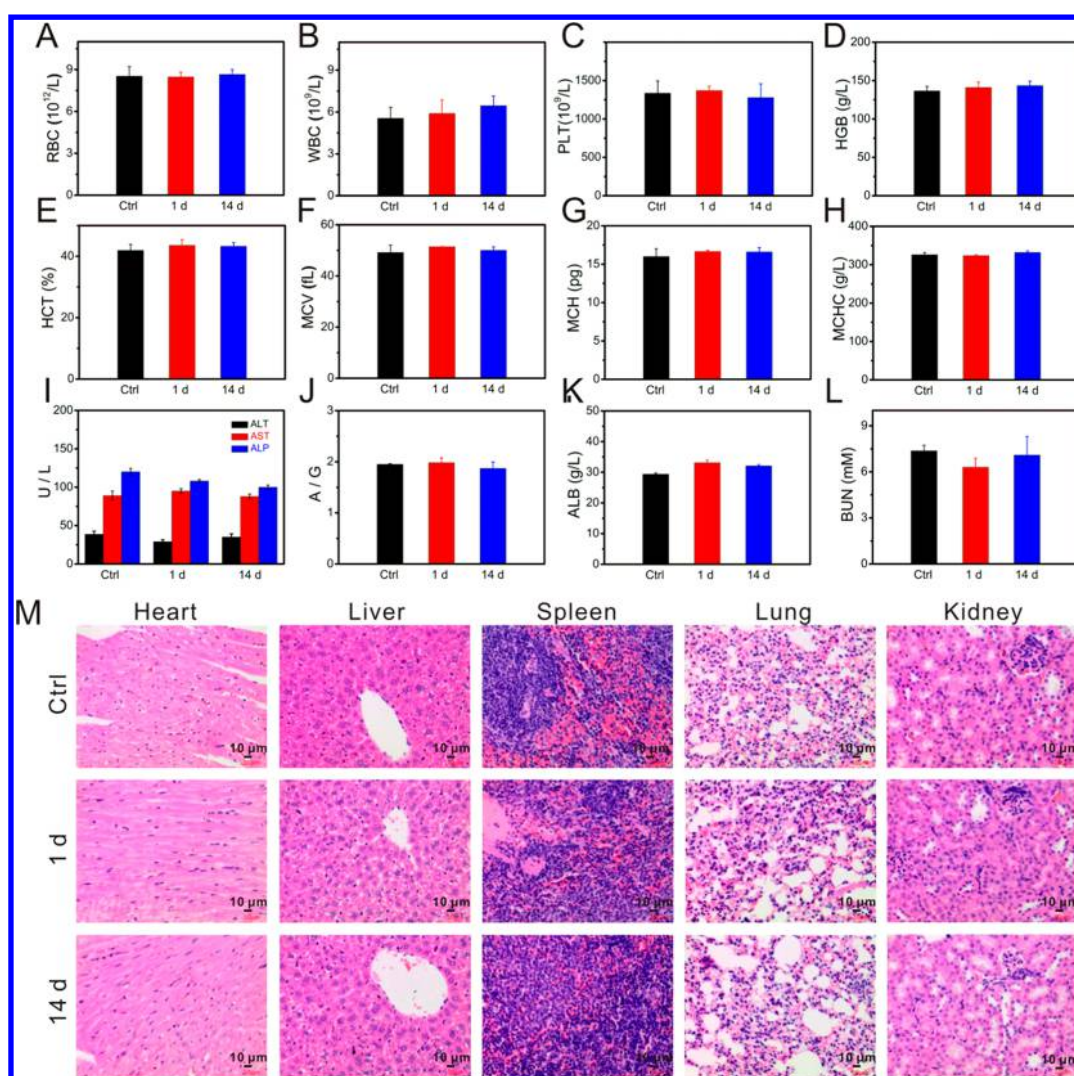
Figure 7. *In vivo* biosafety evaluations of Gd@HRP[ABTS] nanodots after intravenous injection at a dosage of 20 mg/kg. (A−H) blood routine examination, including (A) RBC, (B) WBC, (C) PLT, (D) HGB, (E) HCT, (F) MCV, (G) MCH, and (H) MCHC. (I−L) Blood biochemistry test, containing (I) ALT, ALP, AST, (J) A/G, (K) ALB, and (L) BUN. (M) H&E-stained images of main organ tissues of the mice, such as heart, liver, spleen, kidney, and lung harvested from the control and the treated 1 and 14 days after intravenous injection of Gd@HRP[ABTS] nanodots (100×).

allows for more time to do treatment and eventually improves the therapeutic effect.

MR imaging demonstrates the good tumor uptake of Gd@HRP[ABTS]. Subsequently, PA imaging was carried out before and after intravenous injection of Gd@HRP[ABTS] at different time points. As shown in Figure 5A,C, the PA signal intensity reaches a maxima at 2 h post-injection, and after that, the signal intensity decreases. This enhancing pattern is very similar to that under the MR imaging mode. The PA imaging results also suggest the good tumor accumulation of Gd@HRP[ABTS] nanodots. The aroused PA signals in the tumor confirm that the stowed ABTS can be catalytically oxidized by the HRP moiety of the loading carrier (Gd@HRP) in the presence of the endogenous H_2O_2 in the tumor microenvironment. Obviously, like MR imaging, the potent H_2O_2-trggered PA imaging can be also used to guide the PTT as well.

Besides imaging the tumor sites, the biodistribution of Gd@HRP[ABTS] nanodots in other main organs such as liver, kidneys, and bladder was measured *in vivo* under the MR imaging mode. It shows that compared with pre-injection, MR signal in the liver

is gradually enhanced post-injection and reaches a maximum at 2 h post-injection. But after 2 h, the signal in liver decreases gradually (Figure 5D). Compared with other previously reported nanosized contrast agents that usually accumulated in the liver for over 24 h,[36,37] Gd@HRP[ABTS] nanodots present a rapid metabolism from the liver, in favor of reducing the toxicity of nanoparticles accumulated in body. The MR enhancement patterns of Gd@HRP[ABTS] nanodots in kidneys and bladder were found very similar to that in the liver (Figure 5E,F). T_1 hyperintensities both in kidneys and bladder clearly shows that Gd@HRP[ABTS] nanodots can be effectively cleared from the body via kidneys. It is worth noting that kidney-clearable nanoparticles are much more preferred because they could cause less damage or toxicity to the body compared with those only clearable *via* the liver.[38] It is reported that the threshold of nanosize diffusion from the glomerulus is appropriately 6 nm,[39,40] which is close to the size of Gd@HRP[ABTS] nanodots. The excellent water dispersibility of Gd@HRP[ABTS] nanodots also contributes to this clearance pathway. The MR signal intensities of liver, kidney, bladder, and tumor were further

quantified as shown in Figure 5G, which clearly shows a gradient increase to the maximum, and followed by a gradual decrease.

In addition, to further quantify the organ distribution and tumor accumulation efficiency of nanodots, 4T1-tumor bearing mice were intravenously injected by nanodots and sacrificed, and the Gd content at different time points was measured. As displayed in Figure S9 (Supporting Information), it shows that the Gd^{3+} content in the tumor can be as high as ∼7.0% of the injected dose per gram tissue (% ID/g) at 2 h post-injection, indicating a good accumulation of Gd@HRP^{ABTS} nanodots in tumor tissues. This finding is in agreement with the MR/PA imaging results. In addition, a relatively large amount of nanodots were found to be excreted through the kidneys and liver.

***In Vivo* H_2O_2-Tiggered Catalytic PTT.** After understanding the kinetics of Gd@HRP^{ABTS} nanodots in tumor with the assistance of MR/PA imaging guidance, we performed accurate catalytic PTT of tumors. At 2 h post-intravenous injection by Gd@HRP^{ABTS} nanodots, PTT with a procedure of irradiation by an 808 nm NIR laser for 5 min was conducted on tumor-bearing mice. The real-time temperatures at tumor sites were monitored using a thermal imager (Figure 6A). It shows that the tumor temperatures of the mice treated with Gd@HRP^{ABTS} nanodots increase significantly from 27 to 56 °C after 5 min of laser irradiation, which are much higher than those in the control group (physiological saline + laser; Figure 6B). This result suggests the good photothermal conversion effect of the resultant ABTS●+ produced by the HRP-mediated catalytic reaction between ABTS and the intrinsic H_2O_2 in the tumor tissues.

Subsequently, the therapeutic efficacy was assessed by monitoring the change of tumor volume during treatment. As displayed in Figure 6C,D, the tumors of experimental group (Gd@HRP^{ABTS} + 808 nm laser irradiation) exhibit an obvious regression after 3 day of PTT treatments and are almost eliminated on 16 day, while the tumors in the control groups treated with physiological saline, 808 nm laser irradiation only, and Gd@HRP^{ABTS} nanodots only grow rapidly. The relative tumor volumes in the control groups increase by 10−12-fold, compared with pretreatment. The results from these comparing experiments suggest the potent PTT efficacy of Gd@HRP^{ABTS} nanodots. This is further evidence that the HRP on the Gd@HRP^{ABTS} nanodots still retains its enzymatic activity to catalytically oxidize ABTS into photoactive ABTS●+.

In addition, the body weights of the experimental group mice do not exhibit a downward trend throughout the experiment (Figure 6E), indicating no severe systemic side effects during PTT. This low side effects of PTT are mainly due to TME-triggered PTT, which is tumor specific and can reduce phototoxicity to the adjacent normal tissues.

To further investigate the therapeutic efficacy, the tumor tissues were harvested after different treatments and analyzed by using H&E staining. As presented in Figure 6F, the tumor tissue treated with Gd@HRP^{ABTS} nanodots plus 808 nm laser irradiation shows obvious necrosis, and the tumor cellular shape becomes much more irregular with shrinking nuclei compared with those in the other control groups.

***In Vivo* Toxicology Analysis.** To investigate the safety of the prepared Gd@HRP^{ABTS} nanodots, blood routine analysis, blood biochemistry test, and H&E staining examination were conducted at 1 and 14 days post-intravenous injection of Gd@HRP^{ABTS} nanodots (dosage: 20 mg/kg). As shown in Figure 7A−H, the blood routine examination results demonstrate no noticeable changes in the main blood parameters, such as HGB, RBC, MCHC, HCT, WBC, MCV, PLT, and MCH, indicating good hemocompatibility of Gd@HRP^{ABTS}. The biochemistry test results demonstrate that the liver injury markers (ALP, AST, and ALT), indicators of kidney injury (BUN), and serum levels (A/G, ALB) of the mice treated with Gd@HRP^{ABTS} were comparable to those of the control group, suggesting low or no damage to either the kidneys or the liver (Figure 7I−L). Moreover, H&E staining examination of major organs, including heart, spleen, kidney, liver, and lung, was carried out to further assess *in vivo* toxicity of Gd@HRP^{ABTS} nanodots. As displayed in Figure 7M, compared with the control group (physiological saline injection), the tissue structures of the mice after 14 days of Gd@HRP^{ABTS} treatment are found to be almost intact, and no noticeable cell necrosis, organ damage, or inflammatory lesions can be detected. Thus, it could be concluded that the bioinspired Gd@HRP^{ABTS} nanodots are probably safe in living mice. Undeniably, before translational use, more toxicology evaluation should be done.

CONCLUSIONS

In conclusion, we demonstrate HRP-assisted biomimetic synthesis of ultrasmall nanodots while simultaneously retaining high enzymatic activity for tumor-selective catalytic photo-theranostics. In this study, HRP has multiple roles: a biotemplate for Gd-based nanodots formation and stabilization, a carrier for ABTS loading, and particularly a catalyst for catalyzing the oxidation of the stowed ABTS. It was found that (1) HRP produced high-quality Gd@HRP^{ABTS} nanodots and simultaneously preserved *ca.* 70% of catalytic activity; (2) the effect of NaOH on enzymatic activity was larger than that of Gd^{3+} ions; and (3) the effect of NaOH can be erased by adjusting pH. Based on these features, Gd@HRP^{ABTS} nanodots not only show good tumor targeting but also exert efficient catalytical oxidation of ABTS substrate into photosensitive counterparts by the intrinsic H_2O_2 inside the tumor, enabling a tumor-specific PA/PTT. Furthermore, the ultrasmall Gd@HRP^{ABTS} nanodots were found clearable *via* kidneys without any noticeable toxicity. The proposed work, we believe, could be of great relevance for inspiring other functional proteins or enzymes for multirole biomimetic synthesis while simultaneously retaining their intrinsic properties for cancer targeting, signal generation, or catalytic.

EXPERIMENTAL SECTION

Materials. Horseradish peroxidase (HRP), hydrogen peroxide solution (H_2O_2, 30 wt % in H_2O), and 2,2′-Azinobis (3-ethyl-benzothiazoline-6-sulfonic acid ammonium salt) (ABTS) were purchased from Aladdin. Gadolinium chloride hexahydrate ($GdCl_3$·$6H_2O$) was ordered from Sigma-Aldrich. Sodium hydroxide (NaOH) and phosphate buffered saline (PBS) were obtained from Sinopharm. Chemical Reagent Co., Ltd. (Shanghai, China). Cell Counting Kit-8 (CCK-8) was ordered from KeyGEN bioTECH (Nanjing, China). All chemicals were used without further purification, and deionized water (18.2 MΩ·cm resistivity at 25 °C) was used throughout the study.

Materials Characterizations. The morphology and size of Gd@HRP^{ABTS} nanodots were observed by high-resolution transmission electron microscopy (HRTEM) operated at a voltage of 200 kV. The X-ray photoelectron spectroscopy (XPS) measurements were carried out on PHI-5000 CESCA system (PerkinElmer) with radiation of Al K$_\alpha$ (1486. Six eV) X-ray source. The hydrodynamic diameter (HD) and UV−vis absorption spectrum of Gd@HRP^{ABTS} were measured by dynamic light scattering (Malvern) and Cary 50 spectrophotometer (Varian), respectively. Circular dichroism (CD) spectra and

endogenous fluorescence of pure HRP, Gd^{3+}+HRP, HRP + NaOH, and Gd@HRP^{ABTS} were measured by spectropolarimeter system (BioLogic, MOS-450) and fluorescence spectrophotometer (Cary Eclipse, Agilent), respectively. The Gd concentration was determined by inductively coupled plasma-atomic emission spectroscopy (ICP-AES) on a Thermal Scientific (iCAP 7400).

HRP-Assisted Biomimetic Synthesis of Gd@HRP^{ABTS} Nanodots. *Gd@HRP Synthesis.* The Gd@HRP^{ABTS} nanodots were synthesized by a biomimetic mineralization strategy according to the previous reports.[22] Briefly, 10 mg of HRP powder was dissolved in 1 mL of ultrapure water, followed by mixing with 50 μL of $GdCl_3 \cdot 6H_2O$ (100 mM) under magnetic stirring at 37 °C. After 3 min, 50 μL of sodium hydroxide solution (NaOH, 1.0 M) was added to adjust the pH to 11–12. Then, the reaction was allowed to proceed at 37 °C for 6 h. Finally, the obtained light brown solution was dialyzed for 24 h against ultrapure water to remove excess ions.

Gd@HRP^{ABTS} Synthesis. One mL of ABTS (10 mg/mL) was added into the above Gd@HRP solution. After incubating for 24 h in the dark, the Gd@HRP^{ABTS} nanodots were purified and concentrated through ultrafiltration at least three times. Finally, the obtained precipitation was redispersed in ultrapure water for further use.

Relaxivity Measurement and *in Vitro* MR Imaging. The relaxation time, including longitudinal (T_1) and transverse (T_2) times of Gd@HRP^{ABTS}, and commercial Magnevist (Gd-DTPA) were measured using a minispec mq 60 NMR Analyzer (1.41 T, Bruker) at 37 °C. Then, the slope of curves that fit the $1/T_1$ and $1/T_2$ (s^{-1}) *versus* Gd^{3+} concentration (mM) were obtained, which represent longitudinal (r_1) and transverse (r_2) relaxation rates, respectively.

The *in vitro* T_1-weighted MR images of Gd@HRP^{ABTS} and commercial Magnevist (Gd-DTPA) were obtained from NM42-040H-I Analyzer. The detailed parameters were set as follows: T_1-weighted sequence, spin echo, FOV = 80 mm × 80 mm, slice gap = 0.55 mm, matrix acquisition = 90 × 90, TR/TE = 500/18.2 ms, slice width = 5.0 mm, NS = 2, slices = 8.

In Vitro H$_2$O$_2$ Response Study. 100 μL of Gd@HRP^{ABTS} nanodots (4 mg/mL) was mixed with different concentrations of H_2O_2 (0 μM, 5 μM, 15 μM, 25 μM, 50 μM, and 100 μM), respectively. Then, the absorption spectra, photothermal conversion effect irradiated by a NIR laser (808 nm, 1.0 W/cm^2), and photoacoustic imaging effect were measured.

Cytotoxicity Study. 4T1 breast cancer cells were cultured in DMEM (Gibco, USA) supplemented with 1% penicillin streptomycin (PS) and 10% fetal bovine serum (FBS) in the presence of 5% CO_2 at 37 °C. All of the cell lines used in this work were obtained from Shanghai Institute of Cells, Chinese Academy of Sciences.

The cytotoxicity of Gd@HRP^{ABTS} nanodots was evaluated *via* a standard cell counting kit-8 (CCK-8) assay. Briefly, 4T1 breast cancer cells (~8000/well) were seeded into a 96-well microplate and permitted to adhere overnight (37 °C, 5% CO_2). Then, the culture medium was replaced by fresh culture medium containing Gd@HRP^{ABTS} nanodots at different concentrations (0, 30, 60, 100, 250, and 500 ppm), respectively. After incubation for 24 h, the culture medium was replaced by 100 μL of pure medium containing 10 μL of CCK-8. After incubating for an additional 2 h, the absorbance at 450 nm was measured using a microplate reader. The cell viability was then calculated according to comparing the absorbance at λ = 450 nm with the control groups. The cytotoxicity of H_2O_2 (0−100 μM) was also investigated according to a similar method.

H$_2$O$_2$-Triggered Photothermal Therapy on Tumor Cells. 4T1 breast cancer cells were incubated with Gd@HRP^{ABTS} nanodots (500 ppm) and H_2O_2 (100 μM) for 2 h, followed by laser irradiation for 5 min. The temperature was monitored by a thermal imager (FLIR). The cells treated with laser irradiation only were set as the control. The cell viability was then calculated according to comparing the absorbance at λ = 450 nm with the control groups.

Tumor Model Construction and *in Vivo* MR/PA Imaging Study. *Tumor Model Construction.* *In vivo* animal experiments were performed in accordance with a standard guideline approved by the Institutional Animal Care and Use Committee of Tong ji University. Typically, 4T1 mice breast cancer cells (~1 × 10^6), suspended in 100

μL of PBS, were injected subcutaneously into the right thigh of each Balb/c mouse (22 g, 5 week old, female) to establish the tumor model.

In Vivo MR Imaging. 4T1 tumor-bearing mice were anesthetized with pentobarbital sodium (1%, 140 μL) and then scanned on Ingenia 3.0 T MR imaging system (PHILIPS, Shanghai Public Health Clinical Center, China). After obtaining the background MR images, the mice were intravenously injected with Gd@HRP^{ABTS} nanodots dispersed in normal saline (dose: 0.08 mmol Gd/kg). Then, the MR images of tumor, liver, kidney, and bladder were recorded at different post-injection time points (0.5, 1, 2, 4, 6, and 24 h). The scanning parameters were set as follows: TR/TE = 600/20, FOV read = 90 mm, FOV phase = 90 mm, ST = 1.2, Slice pos = 12.9, slice width = 3.5 mm, flip angle = 90°, slice gap = 0.5 mm.

In Vivo PA Imaging. 4T1 tumor-bearing mice were anesthetized with pentobarbital sodium (1%, 120 μL), followed by scanning on an animal photoacoustic imaging system (Endra Nexus 128, USA). After obtaining the background PA images, the mice were intravenously injected with Gd@HRP^{ABTS} nanodots dispersed in normal saline. Then, PA signals of tumor site at different post-injection time points (0.5, 1, 2, 4, 6, and 24 h) were detected at an excitation wavelength of 800 nm.

In Vivo H$_2$O$_2$-Triggered Catalytic Photothermal Therapy. Balb/c tumor bearing mice (tumor volume: ~100 mm^3) were randomly divided into four groups (n = 4), followed by receiving different treatments: (1) normal saline injection; (2) laser irradiation only (808 nm, 1.5 W/cm^2); (3) Gd@HRP^{ABTS} nanodots injection (dosage: 10 mg/kg); and (4) Gd@HRP^{ABTS} nanodots injection (dosage: 10 mg/kg) plus laser irradiation (808 nm, 1.5 W/cm^2). The local tumor temperatures and thermal images during laser irradiation were obtained by a thermal imager (FLIR). Then, the tumor size and body weight of mice were monitored by a caliper and electronic balance every other day. The tumor volumes were calculated according to the following formula: length × width^2/2. After therapy, the mice were sacrificed, and the tumors were collected for H&E staining analysis.

In Vivo Toxicity Analysis. *Blood Toxicology Analysis.* Healthy Balb/c mice (n = 5, 5 week old, female, Shanghai Slac) were intravenously injected with Gd@HRP^{ABTS} nanodots (doge: 20 mg/kg). Then, the mice were anaesthetized at 1 and 14 days post-injection, and the blood was collected after removing the eyeballs for routine blood (whole blood) and biochemistry (serum) detection at Shanghai Model Organisms Center, Inc. The mice treated with normal saline were set as the control group.

Organ Toxicology Analysis. After dissection, the main organs of the above-mentioned mice, such as liver, lung, heart, kidney, and spleen, were collected and fixed with tissue fixative. Then, the fixed tissues experienced dehydration, embedment, section (thickness: 4 μm), and staining with hematoxylin and eosin (H&E). Finally, H&E stained images of organs were observed and obtained with a digital microscope. The mice treated with normal saline were set as the control group.

ASSOCIATED CONTENT

ⓢ Supporting Information

The Supporting Information is available free of charge on the ACS Publications website at DOI: 10.1021/acsnano.8b05797.

> Optimized HRP amount for synthesis of nanodots, standard curve of ABTS, photostability evaluation, transverse relaxation rate of Gd@@HRP^{ABTS} nanodots, HRP enzyme activity investigation after laser irradiation, and *in vivo* biodistribution behavior of Gd@@HRP^{ABTS} nanodots (PDF)

AUTHOR INFORMATION

Corresponding Author

*E-mail: bingbozhang@tongji.edu.cn.

ORCID ⓘ

Xin Zhou: 0000-0002-5580-7907

Bingbo Zhang: 0000-0002-0981-7071

Notes

ACKNOWLEDGMENTS

REFERENCES

(1) Yang, T.; Tang, Y. A.; Liu, L.; Lv, X. Y.; Wang, Q. L.; Ke, H. T.; Deng, Y. B.; Yang, H.; Yang, X. L.; Liu, G.; Zhao, Y. L.; Chen, H. B. Size-Dependent Ag$_2$S Nanodots for Second Near-Infrared Fluorescence/Photoacoustics Imaging and Simultaneous Photothermal Therapy. *ACS Nano* **2017**, *11*, 1848−1857.

(2) Xie, J.; Zheng, Y.; Ying, J. Y. Protein-Directed Synthesis of Highly Fluorescent Gold Nanoclusters. *J. Am. Chem. Soc.* **2009**, *131*, 888−889.

(3) Yang, W. T.; Guo, W. S.; Le, W. J.; Lv, G. X.; Zhang, F. H.; Shi, L.; Wang, X. L.; Wang, J.; Wang, S.; Chang, J.; Zhang, B. B. Albumin-Bioinspired Gd:CuS Nanotheranostic Agent for *In Vivo* Photoacoustic/Magnetic Resonance Imaging-Guided Tumor-Targeted Photothermal Therapy. *ACS Nano* **2016**, *10*, 10245−10257.

(4) Yang, W.; Guo, W.; Chang, J.; Zhang, B. Protein/Peptide-Templated Biomimetic Synthesis of Inorganic Nanoparticles for Biomedical Applications. *J. Mater. Chem. B* **2017**, *5*, 401−417.

(5) An, F.-F.; Zhang, X.-H. Strategies for Preparing Albumin-based Nanoparticles for Multifunctional Bioimaging and Drug Delivery. *Theranostics* **2017**, *7*, 3667−3689.

(6) Abbas, M.; Zou, Q.; Li, S.; Yan, X. Self-Assembled Peptide- and Protein-Based Nanomaterials for Antitumor Photodynamic and Photothermal Therapy. *Adv. Mater.* **2017**, *29*, 1605021.

(7) Gao, F.; Cai, P.; Yang, W.; Xue, J.; Gao, L.; Liu, R.; Wang, Y.; Zhao, Y.; He, X.; Zhao, L.; Huang, G.; Wu, F.; Zhao, Y.; Chai, Z.; Gao, X. Ultrasmall [^{64}Cu]Cu Nanoclusters for Targeting Orthotopic Lung Tumors Using Accurate Positron Emission Tomography Imaging. *ACS Nano* **2015**, *9*, 4976−4986.

(8) Yang, W.; Wu, X.; Dou, Y.; Chang, J.; Xiang, C.; Yu, J.; Wang, J.; Wang, X.; Zhang, B. A Human Endogenous Protein Exerts Multi-Role Biomimetic Chemistry in Synthesis of Paramagnetic Gold Nanostructures for Tumor Bimodal Imaging. *Biomaterials* **2018**, *161*, 256−269.

(9) Kwon, K. C.; Jo, E.; Kwon, Y.-W.; Lee, B.; Ryu, J. H.; Lee, E. J.; Kim, K.; Lee, J. Superparamagnetic Gold Nanoparticles Synthesized on Protein Particle Scaffolds for Cancer Theragnosis. *Adv. Mater.* **2017**, *29*, 1701146.

(10) Yang, T.; Ke, H.; Wang, Q.; Tang, Y. a.; Deng, Y.; Yang, H.; Yang, X.; Yang, P.; Ling, D.; Chen, C.; Zhao, Y.; Wu, H.; Chen, H. Bifunctional Tellurium Nanodots for Photo-Induced Synergistic Cancer Therapy. *ACS Nano* **2017**, *11*, 10012−10024.

(11) Chen, Q.; Feng, L. Z.; Liu, J. J.; Zhu, W. W.; Dong, Z. L.; Wu, Y. F.; Liu, Z. Intelligent Albumin-MnO$_2$ Nanoparticles as pH-/H$_2$O$_2$-Responsive Dissociable Nanocarriers to Modulate Tumor Hypoxia for Effective Combination Therapy. *Adv. Mater.* **2016**, *28*, 7129.

(12) Wang, Y.; Wu, Y.; Liu, Y.; Shen, J.; Lv, L.; Li, L.; Yang, L.; Zeng, J.; Wang, Y.; Zhang, L. W.; et al. BSA-Mediated Synthesis of Bismuth Sulfide Nanotheranostic Agents for Tumor Multimodal Imaging and Thermoradiotherapy. *Adv. Funct. Mater.* **2016**, *26*, 5335−5344.

(13) Yang, T.; Wang, Y.; Ke, H.; Wang, Q.; Lv, X.; Wu, H.; Tang, Y.; Yang, X.; Chen, C.; Zhao, Y.; Chen, H. Protein-Nanoreactor-Assisted Synthesis of Semiconductor Nanocrystals for Efficient Cancer Theranostics. *Adv. Mater.* **2016**, *28*, 5923.

(14) Sheng, J.; Wang, L.; Han, Y.; Chen, W.; Liu, H.; Zhang, M.; Deng, L.; Liu, Y.-N. Dual Roles of Protein as a Template and a Sulfur Provider: A General Approach to Metal Sulfides for Efficient Photothermal Therapy of Cancer. *Small* **2018**, *14*, 1702529.

(15) Zhen, X.; Xie, C.; Pu, K. Temperature-Correlated Afterglow of a Semiconducting Polymer Nanococktail for Imaging-Guided Photothermal Therapy. *Angew. Chem.* **2018**, *130*, 4002−4006.

(16) Lyu, Y.; Zeng, J.; Jiang, Y.; Zhen, X.; Qiu, S.; Wang, T.; Lou, X.; Gao, M.; Pu, K. Enhancing Both Biodegradability and Efficacy of Semiconducting Polymer Nanoparticles for Photoacoustic Imaging and Phototheranostics. *ACS Nano* **2018**, *12*, 1801−1810.

(17) Zhu, H.; Fang, Y.; Miao, Q.; Qi, X.; Ding, D.; Chen, P.; Pu, K. Regulating Near-Infrared Photodynamic Properties of Semiconducting Polymer Nanotheranostics for Optimized Cancer Therapy. *ACS Nano* **2017**, *11*, 8998−9009.

(18) Miao, Q.; Xie, C.; Zhen, X.; Lyu, Y.; Duan, H.; Liu, X.; Jokerst, J. V.; Pu, K. Molecular Afterglow Imaging with Bright, Biodegradable Polymer Nanoparticles. *Nat. Biotechnol.* **2017**, *35*, 1102−1110.

(19) Jiang, Y. Y.; Pu, K. Y. Multimodal Biophotonics of Semiconducting Polymer Nanoparticles. *Acc. Chem. Res.* **2018**, *51*, 1840−1849.

(20) Yang, W. T.; Guo, W. S.; Chang, J.; Zhang, B. B. Protein/Peptide-Templated Biomimetic Synthesis of Inorganic Nanoparticles for Biomedical Applications. *J. Mater. Chem. B* **2017**, *5*, 401−417.

(21) Wang, J.; Zhang, B. Bovine Serum Albumin as a Versatile Platform for Cancer Imaging and Therapy. *Curr. Med. Chem.* **2018**, *25*, 2938.

(22) Zhang, B.; Jin, H.; Li, Y.; Chen, B.; Liu, S.; Shi, D. Bioinspired Synthesis of Gadolinium-Based Hybrid Nanoparticles as MRI Blood Pool Contrast Agents with High Relaxivity. *J. Mater. Chem.* **2012**, *22*, 14494−14501.

(23) Szade, J.; Lachnitt, J.; Neumann, M. High-resolution Gd 4d Photoemission from Different Intermetallic Compounds. *Phys. Rev. B: Condens. Matter Mater. Phys.* **1997**, *55*, 1430−1434.

(24) Rahman, A. T. M. A.; Vasilev, K.; Majewski, P. Ultra Small Gd$_2$O$_3$ Nanoparticles: Absorption and Emission Properties. *J. Colloid Interface Sci.* **2011**, *354*, 592−596.

(25) Soderlind, F.; Pedersen, H.; Petoral, R. M.; Kall, P. O.; Uvdal, K. Synthesis and Characterisation of Gd$_2$O$_3$ Nanocrystals Functionalised by Organic Acids. *J. Colloid Interface Sci.* **2005**, *288*, 140−148.

(26) Zheng, X. Y.; Zhao, K.; Tang, J.; Wang, X. Y.; Li, L. D.; Chen, N. X.; Wang, Y. J.; Shi, S.; Zhang, X.; Malaisamy, S.; et al. Gd-Dots with Strong Ligand−Water Interaction for Ultrasensitive Magnetic Resonance Renography. *ACS Nano* **2017**, *11*, 3642−3650.

(27) Cai, X.; Gao, W.; Ma, M.; Wu, M.; Zhang, L.; Zheng, Y.; Chen, H.; Shi, J. A Prussian Blue-Based Core-Shell Hollow-Structured Mesoporous Nanoparticle as a Smart Theranostic Agent with Ultrahigh pH-Responsive Longitudinal Relaxivity. *Adv. Mater.* **2015**, *27*, 6382−6389.

(28) Werner, E. J.; Datta, A.; Jocher, C. J.; Raymond, K. N. High-Relaxivity MRI Contrast Agents: Where Coordination Chemistry Meets Medical Imaging. *Angew. Chem., Int. Ed.* **2008**, *47*, 8568−8580.

(29) Wang, L.; Zhu, X.; Tang, X.; Wu, C.; Zhou, Z.; Sun, C.; Deng, S. L.; Ai, H.; Gao, J. A Multiple Gadolinium Complex Decorated Fullerene as a Highly Sensitive T(1) Contrast Agent. *Chem. Commun.* **2015**, *51*, 4390−4393.

(30) Caravan, P.; Ellison, J. J.; McMurry, T. J.; Lauffer, R. B. Gadolinium (III) Chelates as MRI Contrast Agents: Structure, Dynamics, and Applications. *Chem. Rev.* **1999**, *99*, 2293−2352.

(31) Kadnikova, E. N.; Kostic, N. M. Oxidation of ABTS by Hydrogen Peroxide Catalyzed by Horseradish Peroxidase Encapsulated into Sol-Gel Glass. Effects of Glass Matrix on Reactivity. *J. Mol. Catal. B: Enzym.* **2002**, *18*, 39−48.

(32) Chen, Q.; Liang, C.; Sun, X.; Chen, J.; Yang, Z.; Zhao, H.; Feng, L.; Liu, Z. H$_2$O$_2$-Responsive Liposomal Nanoprobe for Photoacoustic Inflammation Imaging and Tumor Theranostics *via In Vivo* Chromogenic Assay. *Proc. Natl. Acad. Sci. U. S. A.* **2017**, *114*, 5343−5348.

(33) Lin, J.; Zhou, Z.; Li, Z.; Zhang, C.; Wang, X.; Wang, K.; Gao, G.; Huang, P.; Cui, D. Biomimetic One-Pot Synthesis of Gold Nano-

clusters/Nanoparticles for Targeted Tumor Cellular Dual-Modality Imaging. *Nanoscale Res. Lett.* **2013**, *8*, 170.

(34) Zhang, C.; Bu, W.; Ni, D.; Zhang, S.; Li, Q.; Yao, Z.; Zhang, J.; Yao, H.; Wang, Z.; Shi, J. Synthesis of Iron Nanometallic Glasses and Their Application in Cancer Therapy by a Localized Fenton Reaction. *Angew. Chem., Int. Ed.* **2016**, *55*, 2101−2106.

(35) Tang, Z.; Zhang, H.; Liu, Y.; Ni, D.; Zhang, H.; Zhang, J.; Yao, Z.; He, M.; Shi, J.; Bu, W. Antiferromagnetic Pyrite as the Tumor Microenvironment-Mediated Nanoplatform for Self-Enhanced Tumor Imaging and Therapy. *Adv. Mater.* **2017**, *29*, 1701683.

(36) Li, B.; Gu, Z.; Kurniawan, N.; Chen, W.; Xu, Z. P. Manganese-Based Layered Double Hydroxide Nanoparticles as a T_1-MRI Contrast Agent with Ultrasensitive pH Response and High Relaxivity. *Adv. Mater.* **2017**, *29*, 1700373.

(37) Lin, L.-S.; Yang, X.; Zhou, Z.; Yang, Z.; Jacobson, O.; Liu, Y.; Yang, A.; Niu, G.; Song, J.; Yang, H.-H.; Chen, X. Yolk-Shell Nanostructure: An Ideal Architecture to Achieve Harmonious Integration of Magnetic-Plasmonic Hybrid Theranostic Platform. *Adv. Mater.* **2017**, *29*, 1606681.

(38) Ehlerding, E. B.; Chen, F.; Cai, W. Biodegradable and Renal Clearable Inorganic Nanoparticles. *Adv. Sci.* **2016**, *3*, 1500223.

(39) Wang, J.; Liu, G. Imaging Nano-Bio Interactions in the Kidney: Toward a Better Understanding of Nanoparticle Clearance. *Angew. Chem., Int. Ed.* **2018**, *57*, 3008−3010.

(40) Du, B.; Jiang, X.; Das, A.; Zhou, Q.; Yu, M.; Jin, R.; Zheng, J. Glomerular Barrier Behaves as an Atomically Precise Bandpass Filter in a Sub-Nanometre Regime. *Nat. Nanotechnol.* **2017**, *12*, 1096.